Secondary Stability Analysis of Crossflow Vortices using BiGlobal Theory on PIV Base Flows

Groot, Koen; Serpieri, Jacopo; Kotsonis, Marios; Pinna, Fabio

DOI
10.2514/6.2017-1880

Publication date
2017

Document Version
Accepted author manuscript

Published in
55th AIAA Aerospace Sciences Meeting

This is an Accepted Manuscript of an article published in: 55th AIAA Aerospace Sciences Meeting, 9/01/17 - 13/01/17 Grapevine, USA ISBN: 978-1-62410-447-3
Available online: https://arc.aiaa.org/doi/10.2514/6.2017-1880

Secondary Stability Analysis of Crossflow Vortices using BiGlobal Theory on PIV Base Flows

Koen J. Groot*, Jacopo Serpieri†, Marios Kotsonis‡
Delft University of Technology, Delft, 2629HT, The Netherlands
Fabio Pinna§
Von Kármán Institute for Fluid Dynamics, Rhode-St-Genèse, 1640, Belgium

Stability analysis is conventionally applied to highly resolved base flows that are obtained through high-fidelity computational means. Modern experimental methods can capture the flows to higher and higher detail, up to such extent that performing stability analysis thereon has become feasible, at least for specific cases. Secondary instabilities to the primary crossflow vortices in a swept-wing boundary layer are resolved by applying BiGlobal stability theory to the mean flow field measured with tomographic PIV, solving for the high-frequency type I mode dedicatedly. The stability results are found to converge with respect to the mean's ensemble size and are independent of the treatment of the handling of the exterior of the measurement domain. The BiGlobal mode agrees with the instantaneous tomographic PIV and hot-wire anemometry data. This is the first occasion where this approach is applied to this application case. In doing so, one directly avoids problems concerning accounting for the primary vortices' receptivity.

I. Introduction

Swept-wing crossflow-dominated boundary layers are well-known to develop a stationary streamwise crossflow (CF) vortices as a primary instability that modify the mean velocity field. The primary instability is not responsible for the breakdown to turbulence; it is caused by the high-frequency secondary instability.[1–4] Having detailed knowledge about the secondary instabilities, viz. their amplification characteristics and shape, is instrumental in understanding—and ultimately predicting—where laminar-turbulent transition will occur. The classical approach in this regard is the semi-emperical e^N-method,[5] which correlates perturbation amplification to the transition location. Malik *et al.*[6,7] established that this method yields a good transition correlation by applying it to the secondary instability, comparing their results to the experiments of Kohama *et al.*[8] Related experiments are elaborated on by Kawakami *et al.*,[9] Bippes & Lerche[10] and Bippes.[11] Kawakami *et al.*[9] and Chernoray *et al.*[12] performed phase-locked hot-wire measurements. In the recent work of Glauser *et al.*[13] a transition correlation is proposed with respect to the onset of the POD modes detected by wall-mounted hot-films.

The main effect of the primary CF vortices on the base flow is to redistribute momentum by advection about their vortical axis. The resulting instantaneous and mean flow therefore has large shear stress components in two, as opposed to one, spatial directions. Perturbations that are generated under these conditions can be approached using linear stability theory and are governed by the BiGlobal stability equations,[14] investigations of this type for this application are applied by Malik *et al.*,[6] Högberg & Henningson[15] and Wasserman & Kloker.[16] This is a system of two dimensional partial differential equations (PDEs), that takes into account all the base flow's inhomogeneities, i.e. shear stress, in a plane. Different approaches to the secondary instability involve Floquet theory[17–19] and DNS.[1,16] The most prominent secondary modes are classified into three catagories by Koch *et al.*[19] First, the high-frequency type I mode is related to the

*Ph.D. student, Faculty of Aerospace Engineering, k.j.groot@tudelft.nl
†Ph.D. student, Faculty of Aerospace Engineering, j.serpieri@tudelft.nl
‡Assistant professor, Faculty of Aerospace Engineering, m.kotsonis@tudelft.nl
§Research engineer, Von Kármán Institute for Fluid Dynamics, fabio.pinna@vki.ac.be

spanwise shear layer in the upwash region of the primary vortex. Second, the high-frequency type II mode lives on top of the vortex and is mainly produced by wall-normal shear. Third, the type III mode resides close to the wall under the primary vortex, due to the low local convection velocities it is dominant at low frequencies. Malik *et al.*[20] have also termed the type I and II modes as z- and y-modes corresponding to the dominant direction in the shear layer they inhabit.

The primary CF vortices have receptivity mechanisms of their own; they are sensitive to the specific disturbance environment, e.g. micron-sized surface roughness near the leading edge and freestream turbulence. The secondary stability analysis, in turn, depends strongly on the primary vortices and the overall disturbance environment, so care must be taken in representing the base flow for the secondary stability analysis. This complication is avoided by directly measuring the base flow and perform the stability analysis thereon. This is the main focus of this paper; applying the BiGlobal stability theory to a base flow that is conceived through experimental means. and the primary crossflow vortices to determine the secondary instability. Usually the latter is approached numerically by performing NPSE or DNS, that require careful recepticity calibration for the initial condition, see Malik *et al.*,[7] Fisher & Dallmann[21] and Bonfigli & Kloker.[1] The current approach has also been applied to the flow about a micro-ramp; a type of micro vortex generator.[22]

The approach is to use an experimentally measured "base flow" for the secondary stability analysis using tomographic (or tomo-)PIV, capturing the boundary layer flow and the mean flow distortion effect due to the primary vortex. The base flow is represented by forming the mean of instantaneous snapshots under the hypothesis that the difference between the base and mean flow becomes negligible as the number of instantaneous snapshots is increased. The field of view of the measurement is limited, which is approached by simple extrapolations using Blasius profiles. In the same vein, the shear layer under the primary vortex in the raw tomo-PIV data displays erroneous inflection points because it is difficult to measure near the wall.[23] This is mended with the only objective to avoid highly unstable artificial solutions. The solutions of interest are found to be independent of these features as they have nearly zero amplitude outside the field of view. The set-up of the tomo-PIV and hot-wire experiments and the pre-processing of the experimental data will be elaborated on in detail in Sec. II. The used experimental results are published independently, see Serpieri & Kotsonis[24] for a treatment of the tomo-PIV experiments and Serpieri & Kotsonis[25] for the hot-wire experiments.

The main objective is to investigate whether the secondary instabilities of interest can be approached using BiGlobal stability theory on experimental base flows. The numerics of the BiGlobal stability method is discussed in secion III The focus of the verification lies on the independency to the ensemble size for the mean and the handling of the near-wall and freestream regions. A validation is performed in Sec. IV using the instantaneous experimental data, relying on the comparison of the flow structures with those obtained with hot-wire and tomo-PIV measurements. To this end, the BiGlobal modes are simply extracted at the measured frequencies and determined at the fixed 45% chord location; determining amplification curves or performing transition correlations are out of the current scope. The verification and validation are elaborated on in Sec. IV and discussed in Sec. V. The paper is concluded in Sec. VI.

II. Experimental Base Flow

The base flow is the mean field obtained with three-dimensional tomo-PIV measurements of which the experimental set-up is the same as that elaborated upon by Serpieri & Kotsonis;[24] the main difference in the case of the hot-wire experiment is the inclusion of the DBD plasma actuator. See Fig. 1(left) for schematics of the hot-wire and tomo-PIV set-ups. The experiment was performed in the TU Delft LTT facility. The model is a 45° swept wing with an airfoil that is an adaptation of the NACA66018 shape, called 66018M3J, with a small leading edge radius to avoid attachment line instability, see Fig. 1(top right). The angle of attack of the wing was set to 3 degrees, so to enhance the crossflow instability at the pressure side. At this angle of attack, the pressure minimum is attained at $X/c_X = 0.63$, where X is parallel to the tunnel walls and c_X the chord in the X-direction. The full C_p-distribution is shown in Fig. 1(bottom right). The windtunnel inflow velocity is $\overline{Q}_\infty = 25.6\,[m/s]$, yielding a chord Reynolds number of $2.17 \cdot 10^6$. The measurement is performed about the 45% chord, spanwise center location. At this location, the vortices and inviscid streamline respectively have an angle of 5.0 and 1.74 degrees (clockwise positive) with $\overline{Q}_\infty$.

Several coordinate systems are defined, as illustrated in Fig. 2. The first, (X, Y, Z), has X parallel to $\overline{Q}_\infty$, Z in the spanwise direction perpendicular to the tunnel walls and Y normal to the ZX-plane. The second, (x_w, y, z_w), is aligned with the primary crossflow vortices. I.e. x_w is parallel to the vortices, y

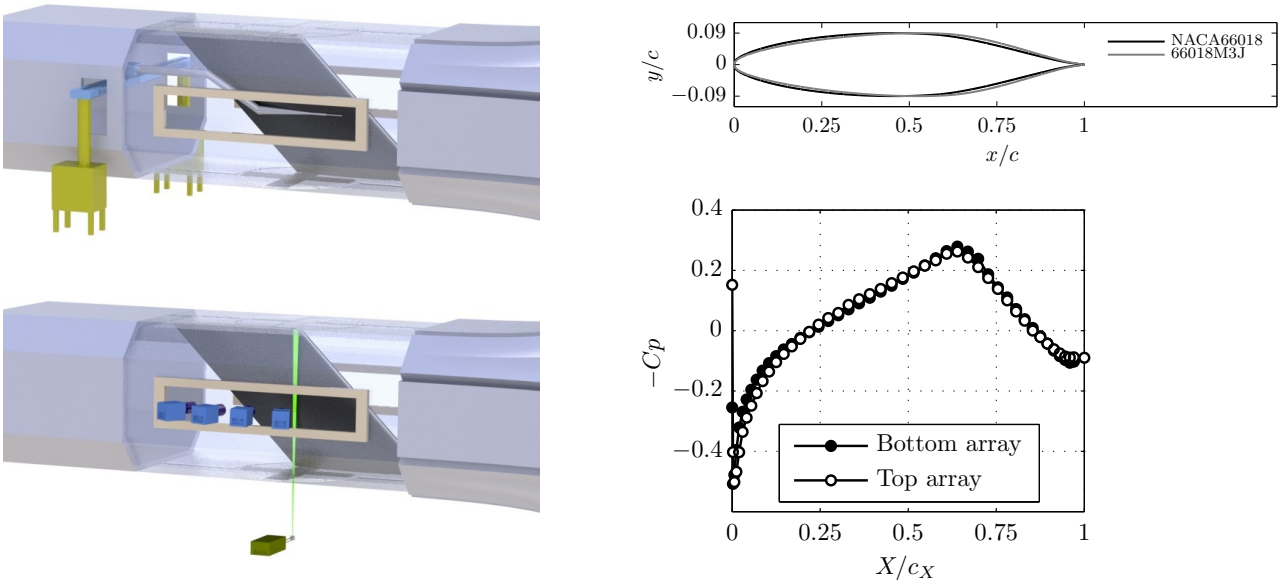

Figure 1. Schematic of the (top left) hot-wire and (bottom left) tomo-PIV set-up, the flow comes from right. (top right) 66018M3J and NACA66018 airfoils. (bottom right) C_p-distribution of the 66018M3J airfoil. Reproduced from Serpieri & Kotsonis.[24]

wall-normal with respect to the airfoil and z_w spanwise, perpendicular to the $x_w y$-plane. With exceptions, this will be the main coordinate system used to display the results. The related velocity components are indicated with the subscript w. The third (swept-wing) coordinate system, (x, y, z), is obtained by rotating the (X, Y, Z)-system 45° about the Y-axis. x is orthogonal to the leading edge, y wall-normal with respect to the airfoil and z parallel to the leading edge. The origin in the (x_w, y, z_w)- and (x, y, z)-systems is placed at the 45% chord, spanwise center position. In the experimental treatments, the y-coordinate normal to the airfoil is also denoted by y_t; at the fixed streamwise station of current interest, $X/c_X = 45\%$, the difference is negligible. The primary instability is fixed by installing a cylindrical roughness element array at $X/c_X = 2.5\%$ parallel to the leading edge, with a spanwise spacing of $9\,[mm]$. The elements' diameter and height are $2.8\,[mm] \times 10\,[\mu m]$. The projection of the roughness spacing on the z_w-direction is $9\cos 40° = 6.89\,[mm]$. This length is denoted by λ_r and used as the length scale throughout. The edge velocity in the direction of the primary vortex at $X/c_X = 45\%$, $\overline{U}_{w,e}$, is $28.0\,[m/s]$. This is used as the velocity scale throughout the paper and is denoted with $\overline{U}_e$ in the remainder.

II.A. Tomographic PIV

The tomo-PIV setup consisted of four cameras, that were mounted in an arc configuration located approximately one meter away from the model (see Fig. 1(left)). The laser light enters the wind tunnel vertically from below. The final field of view was $35 \times 35 \times 3\,[mm^3]$ and centered at $X/c_X = 0.45$. Volume reconstruction and correlation were performed in a coordinate system aligned with the primary crossflow vortices, i.e. in the x_w-direction. The final interrogation volume size is $2.6 \times 0.67 \times 0.67\,[mm^3]$ in (x_w, y, z_w). For the purposes of this paper it is assumed this yields sufficient spatial resolution. A 75% overlap of adjacent interrogation volumes was used. The final vector field was interpolated on a grid with uniform spacing of $0.15\,[mm]$ in all three directions, only implying interpolation in x_w. The planes were obtained at $x_w = 0$ by a linear interpolation. The measurements were performed at 0.5Hz. Proper Orthogonal Decomposition (POD) analysis is applied to identify the most energetic spatially correlated three-dimensional flow structures.[26] See Serpieri & Kotsonis[24] for more details related to the present application.

In total 500 uncorrelated snapshots were obtained. The mean flow field was conceived with different ensemble sizes (number of snapshots): $N_f = 300$, 400 and 500 are used as a base flow for the stability analysis. Previous studies[22] pointed out that using this amount of snapshots is enough to yield converged stability results. Regarding a maximal perturbation magnitude of $0.1\overline{U}_e$, the uncertainties of the mean fields are estimated to be $0.1/\sqrt{N_f} = 5.8 \cdot 10^{-3}$, $5.0 \cdot 10^{-3}$ and $4.5 \cdot 10^{-3}$ for the 300, 400 and 500 frame cases.

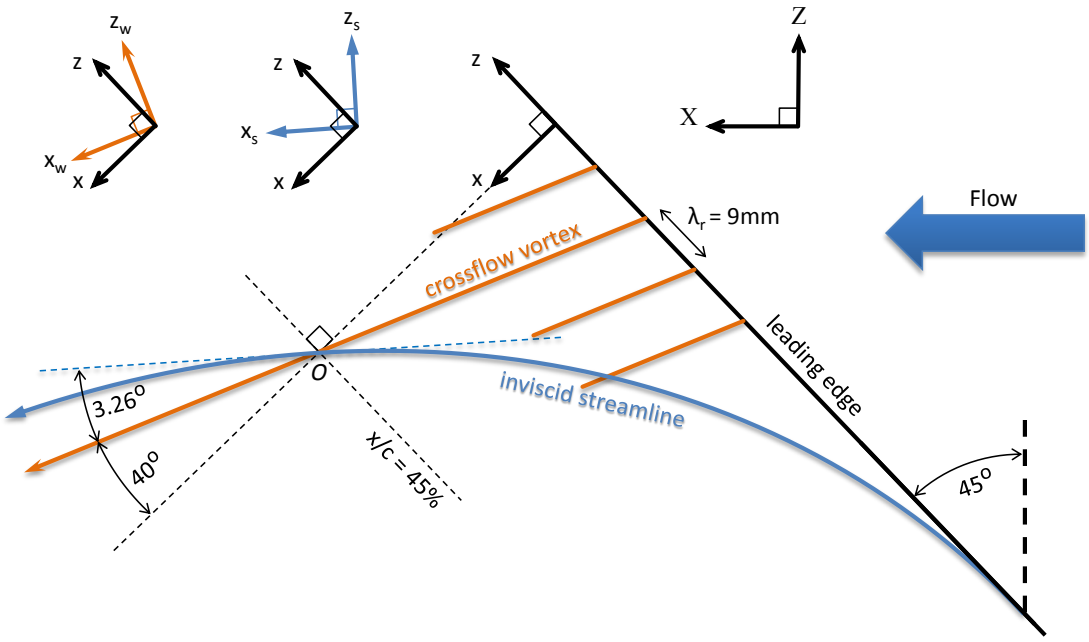

Figure 2. Definition of (left to right) primary crossflow vortex (x_w, z_w), inviscid streamline (x_s, z_s), leading edge (x, z) and freestream (X, Z) coordinate systems. At the 45.0% chord location, the primary vortices have a $-40\circ$ angle with respect to the leading edge orthogonal x-coordinate ($+5.0\circ$ with respect to X), in turn the inviscid streamline has a -3.26° angle with respect to the primary vortices ($+1.74^\circ$ with respect to X).

These are relatively large numbers in terms of the expected uncertainty of the stability analysis, but highly sufficient for PIV standards. Despite of this, the stability results are found to be less sensitive than expected.

The most important feature of the tomo-PIV experiment as opposed to hot-wire measurements, which is the prevalent technique applied in this field,[4,8–13] is that all 3 velocity components are measured in an entire volume. This is the first occasion where such experimental data is available for the current application case. Preliminary BiGlobal stability tests indicated that the results deviated significantly when discarding the in-plane velocity components, despite being an order of magnitude smaller. Lastly, it is noteworthy to mention that the tomo-PIV measurements were performed in a different occasion than the hot-wire experiments. Despite possible differences in the primary CF vortex's receptivity, the current stability results could be reasonably extrapolated to the hot-wire case to compare the structure of the secondary instability.

II.B. Hot-Wire Anemometry

Hot-wire measurements were performed with two probes simultaneously, one for the boundary layer and one for the freestream. The hot-wire was operated at a sampling frequency of $40\,[kHz]$ and low-pass filtered with a cut-off frequency of $15\,[kHz]$ before bridge amplification. The schematic of the total system including the traverse is shown in Fig. 1(left). The sting is not straight so to reduce the influence of the sting on the measurement region. Scans were performed in spanwise planes at $X/c_X = 0.45$ about the spanwise centerplane. The spacing in the wall-normal and Z-direction are $\sim 0.1\,[mm]$ and $0.625\,[mm]$, respectively. The wire was aligned with the Z-direction (vertical in Fig. 1(left)), so that it measured mainly the Euclidean sum of X- and Y-velocity components.

The structure of the perturbation can be constructed in a phase-locked sense if one has knowledge of the phase of the incoming instability. Therefore, the secondary modes are forced with a fixed frequency via a Dielectric Barrier Discharge (DBD) plasma actuator installed on the wing at $X/c_X = 0.30$ parallel to the leading edge, having a measured total thickness of $125\,[\mu m]$. Applications of phase-locked experiments are treated by Kawakami *et al.*[9] and Chernoray *et al.*[12] Oil flow visualization and infrared thermography indicated no adverse effects on the transition location by the actuator's presence. Here the case with forcing frequency $f_f = 4.0\,[kHz]$ is considered, which is proper to the type I mode instability. In combination with the $40\,[kHz]$ sampling frequency, this yields+ 10 measured phases. The obtained data is averaged per phase. These measurements are used solely for the comparison of the mode's structure.

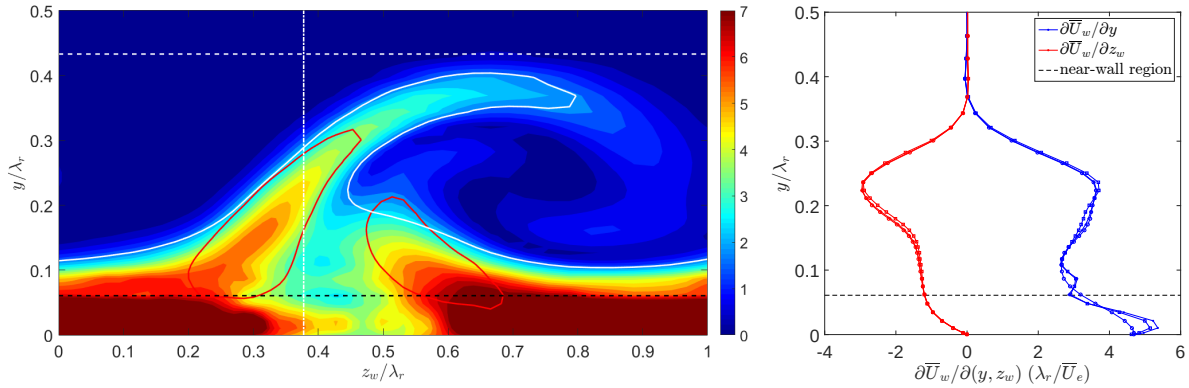

Figure 3. (left) In-plane $\overline{U}_w$-shear magnitude of the 500 frame tomo-PIV dataset, interpolated onto the 55×55 mapped Chebyshev grid. Levels are in units of $\overline{U}_e/\lambda_r$; the maximum encountered above the black dashed line is $7\,\overline{U}_e/\lambda_r$. Red and white thick contours respectively indicate where the z_w- and y-shear magnitudes equal $7/4\,(\overline{U}_e/\lambda_r)$. The horizontal white dashed line ($y/\lambda_r = 0.433$) indicates the highest coordinates captured in the measurement; the black dashed line ($y/\lambda_r = 0.061$) indicates the near-wall region. (right) Shear component profiles for the 500 (solid dots), 400 (circles) and 300 (squares) frame datasets extracted along the vertical dash-dotted line ($z_w/\lambda_r = 0.378$) in the left figure. Black dashed line indicates the near-wall region.

II.C. Pre-Processing for BiGlobal Analysis

Before the mean flow fields can be analysed with the BiGlobal stability method, they have to be pre-processed. This processing is mainly related to the limited field of view and problems associated to measuring in close proximity to the wall.

Regarding the upper limit of the domain, the perturbations need sufficient space to decay in the wall-normal direction, so the $\overline{U}_w$ and $\overline{W}_w$ base flow components are both extrapolated using a Blasius profile, using a cosine weight in an overlap region. In this regard, $\overline{W}_{w,e} = \overline{U}_e \tan 3.26°$, related to the inviscid streamline direction. A Falkner-Skan-Cooke profile would be a better approximation, but for the current purposes using Blasius for $\overline{W}_w$ is deemed sufficient. $\overline{V}$ is extrapolated the same way, approaching zero in the freestream. The height up to which the PIV data is used solely is denoted by δ_{PIV} and the height of the overlap region by Δy.

It is a difficult task to measure near the wall, for which there are several reasons;[23] the most important ones being low particle density, the strong shear near the wall and reflections. Effectively, these features yield the velocity profile to slope off at a non-zero value instead of resembling the no-slip condition. The region where these features are prominent is here referred to as the near-wall region. The type III mode depends sensitively on the flow's details in this region and it is therefore expected to be irreversibly affected by this measurement noise. Moreover, artificial inflection points are created that can cause a significant artificial inviscid instability.

This behaviour is mended with the sole purpose of avoiding the latter solutions. The data closest to the wall is affected most. The treatment is therefore to connect the profiles to the wall, "add" the no-slip condition, and linearly interpolate the data on the y-coordinate closest to the wall using the data on the second y-coordinate. This reduces the artificial shear. In a way, this is analogous to what has been done to suppress the type III mode in the computational literature.[1] The resulting flow field in the near-wall region is in no way the "correct" flow, but now at least can be properly assumed to have no adverse effect on the targeted stability results. The modes of type I and II can be assumed to be affected negligibly. This will be discussed in a larger extent in Sec. V.

The in-plane $\overline{U}_w$-shear from the resulting mean tomo-PIV flow field is shown in Fig. 3(left), using 500 snapshots and extracting the plane along the z_w-coordinate.[24] The spanwise extent of the domain covers one primary vortex in the z_w-direction, $1\lambda_r = 6.89\,[mm]$. Sixth order finite differences are used to determine the derivative fields consistently, i.e. using central differences in the interior and forward/backward differences about the boundaries. This was done to take the most out of the limited resolution. Differentiation is performed with another method than using the mapped Chebyshev matrices to avoid errors in the near-wall region to affect the data at all points in y. It is observed the derivatives of the small quantities $\overline{V}$ and $\overline{W}_w$, that are difficult to measure, can attain large values in the near-wall region and are sensitive to the ensemble size for the mean. Tests are performed in which these levels are artificially reduced, which led to $\mathcal{O}(10^{-4})$

absolute changes in the type I mode's eigenvalues. These features are therefore tolerated. The height of the measurement domain and the near-wall region is shown by the white and black dashed lines respectively. The color scale is adjusted so to remove the levels pertaining to the near-wall region.

It is difficult to spot differences between the analogous contour plots for the different ensemble sizes. To that end Fig. 3(right) displays profiles extracted at constant $z_w/\lambda_w = 0.378$; the location where the type I mode turns out to be most dominant. Although it displays the flow derivative profiles, the fields are similar with the exception of the near-wall region. The largest relative difference between the 400 and 500 frame cases outside of the near-wall region is 1.9% for both profiles. The shear levels are directly related to the modal growth rates,[27] thus one expects the difference in the growth rates to be of this order of magnitude.

III. BiGlobal Stability Analysis

The BiGlobal stability approach assumes the flow to have its shears in 2 principal directions. The flow is assumed to be independent of the third. The best approximation of such a direction in the case of the primary crossflow vortices is along the wave vector of the primary vortices: the x_w-direction. Implicitly this implies one neglects the curvature of the vortices,[1,7] which is a postiori justified by the small wavelengths of the secondary modes.[14] Regarding the spanwise direction, a finite domain extent has to be considered. Here the smallest interesting such length is chosen for simplicity: a single primary vortex wavelength. Moreover, one must justify boundary conditions on the introduced boundaries, especially the periodic boundary conditions in the spanwise direction. The flow is closest to periodic in the leading edge parallel z-coordinate. This implies the BiGlobal plane should be contained in the zy-plane; but the out-of-plane dynamics should be described in terms of quantities pointing in the x_w-direction, non-orthogonal to this plane. This set-up is approached by extracting the base flow at $x = 0.45c$ and projecting it onto an appropriate $z_w y$-plane; effectively changing the spanwise lengthscale. This is explained in high detail by Bonfigli & Kloker,[1] see their Fig. 18 and the corresponding elaboration. Regarding the wall-normal direction, wall conditions[28] are applied at $y = 0$ and Dirichlet conditions are used for all amplitudes on the top boundary as it is located high enough (at $4\lambda_r$) and as it resolves the additive-constant non-uniqueness problem with the pressure.

In the current case, it was chosen not to follow the latter "best" approach regarding the choice of the spanwise coordinate. The $z_w y$-planes were extracted directly from the tomo-PIV data, because the cross-correlation is performed in this direction and hence yields the most consistent representation. The data is interpolated to yield the plane with $z_w = 0$ at $x/c = 0.45$. The introduced non-periodicity is assumed to be negligible. The change in the edge velocity is used as a representative quantity and changes less than 10^{-3} units. This is a consequence of the small chordwise extent of the domain, $9/1270 \sin 40^\circ = 0.0045$. Note, in this regard, that the base flow quantities, including the shear, change discontinuously across the boundaries, but no new shear is introduced due to this.

One combines the aforementioned in the BiGlobal ansatz for the perturbation as follows:

$$q' = \tilde{q}(z_w, y)\, e^{i(\alpha x_w - \omega t)} + c.c. \tag{1}$$

One solves the BiGlobal stability equations for $\omega \in \mathbb{C}$ (given $\alpha \in \mathbb{R}$) or $\alpha \in \mathbb{C}$ (given $\omega \in \mathbb{R}$), the temporal or spatial framework, respectively. In both approaches solutions are sought for which $\omega_r/(2\pi) \approx 4.0\,[kHz]$ and $5.0\,[kHz]$, the frequencies corresponding to the tomo-PIV and hot-wire data, respectively.

The BiGlobal tools of the VKI Extensible Stability and Transition Analysis (VESTA) toolkit are used to set up the stability problem.[29] The problem is discretized using Chebyshev spectral collocation and a BiQuadratic mapping is used to resolve the y- and z_w-directions in specific areas. The BiQuadratic mapping is defined as follows:

$$y = y_{max} \frac{a\eta^2 + b\eta + c}{d\eta^2 + e\eta + f}, \tag{2}$$

$$\begin{array}{ccc} a = (y_{i2} - 3y_{i1}) & b = \frac{3}{2}(y_{i2} - y_{i1}) & c = (y_{i2} + 3y_{i1})/2 \\ d = 2(2y_{i2} - 2y_{i1} - y_{max}) & e = 0 & f = 2y_{max} - y_{i2} + y_{i1} \end{array},$$

where the Chebyshev coordinate $\eta \in [-1, 1]$ and the physical coordinate $y \in [0, y_{max}]$. The mapping is conceived so as to distribute one third of the collocation nodes over the domains $[0, y_{i1}]$, $[y_{i1}, y_{i2}]$ and $[y_{i2}, y_{max}]$, as long as $0 < y_{i1} < y_{i2} < y_{max}$ and $y_{i2} < 9y_{i1}$ and $9y_{i2} < y_{i1} + 8y_{max}$ to ensure a regular one-to-one behaviour. The resulting grids maintain a cosine distribution near the boundaries. In the current context,

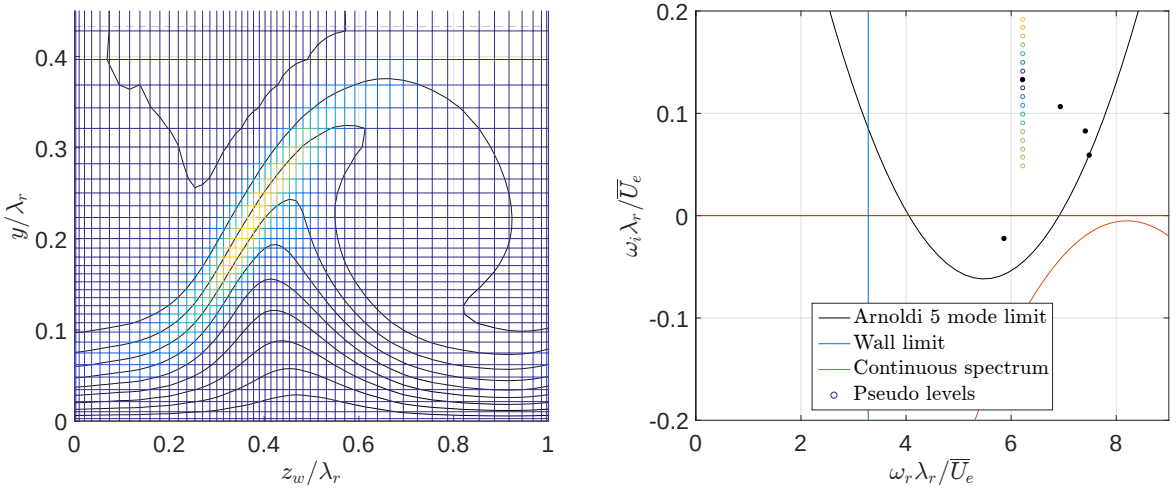

Figure 4. (left) Near wall zoom on optimized grid (55x55 nodes) resolving the type I mode (temporal, $\alpha = 8.2/\lambda_r$) using a BiQuadratic mapping. (right) Resolved eigenvalue region by the Arnoldi algorithm using the optimized shift $\omega_g = (0.669 + 2.02i)\alpha/\overline{U}_e$ to resolve interesting modes only, while avoiding the continuous spectrum and modes dominant in the near-wall region. Particular spectrum corresponds to $\alpha = 8.2/\lambda_r$. Locations about the type I mode where the pseudo levels are resolved are indicated, having a linear spacing of 0.01 units of $\overline{U}_e/\lambda_r$.

the mapping is equipped with specific parameters so to dedicatedly resolve the type I mode. Using $N_z \times N_y = 55 \times 55$ nodes and setting $(z_{i1}, z_{i2}, z_{max}) = (0.30, 0.55, 1.0)\lambda_r$ and $(y_{i1}, y_{i2}, y_{max}) = (0.18, 0.60, 4.0)\lambda_r$ yields the most amplified type I mode to be absolutely converged to $o(10^{-4})$. An example of the mode on the grid is shown in Figure 4(left). Grid convergence was checked by increasing the resolution using these mapping parameters and checking against more conventional grid, applying no or standard bilinear mappings.[30] The type II mode, positioned about the point $(z_w, y) = (0.7, 0.35)$ that is depleted from nodes, has yet to overcome $\mathcal{O}(10^{-3})$ differences with higher resolution computations. Using the BiQuadratic mapping this way has the main advantage of markedly reducing the computational expenses, in terms of RAM and evaluation time, while maintaining excellent accuracy for the main target at hand: the type I mode. The reduced number of nodes rendered both temporal and spatial problems small enough to be solved on small workstations in mass. A single evaluation lasting several minutes.

A final step to improve solving efficiency is setting the center of the resolved spectrum, the parameters for the shift and invert spectral transformation required in the Implicitly Restarted Arnoldi Method (IRAM). This is done considering specific heuristics: the modes of interest are all positioned high in the boundary layer, away from the near-wall region indicated in Figures 3, and they are discrete modes that do not belong to the continuous spectrum. Modes that lie in the near-wall region have low phase speeds corresponding to the low $\overline{U}_w$ values, by inspection smaller than $0.4\overline{U}_e$. Hence, the region with $\omega_r < 0.4\alpha_r$, especially the stable region, is to be avoided. It is indicated in Figure 4(right) as the wall limit. The continuous spectrum contains modes that live in the freestream, those with phase velocity equal to 1. They complete the spectrum, but are very expensive to compute. Due to $\overline{W}_{w,e}$ being non-zero, the upper bound of the spectrum in the ω-plane is the parabola shown in Figure 4(right), with its vertex at $(\alpha(1 - i\alpha/Re)$. The shift is oriented so to equally avoid both (stable) regions, but capture all interesting discrete modes. See Wheeler & Barkley for a similar approach.[31] This allowed reducing the number of resolved modes to 5. Note that this approach results in a large imaginary shift value which occasionally increases the required computational time; a shift closer to the modes is helpful at the cost of having to resolve continuum modes. As one encounters another continuous branch for large negative α_i in the spatial problem, this approach is fruitful only for the temporal problem. Changing the shift or the number of nodes only yields changes of $\mathcal{O}(10^{-12})$.

The pseudospectrum is the generalization of the spectrum indicating regions in the eigenvalue space that might pass for eigenvalues when the problem is subjected to arbitrary perturbations. That is, the ϵ-pseudospectrum contour indicates the maximal perturbation of the eigenvalue when the corresponding operator problem is perturbed by an operator of order ϵ.[32,33] See Riedel[34] for definitions related to generalized problems. Here, the weighted pseudospectrum definition is used; the norms of the right hand side matrices are $\mathcal{O}(1)$. These ϵ contours are used to see where an eigenvalue can be moved subject to the worst-case-scenario ϵ perturbation. Unfortunately, but expectedly, the contours corresponding to the uncertainty levels

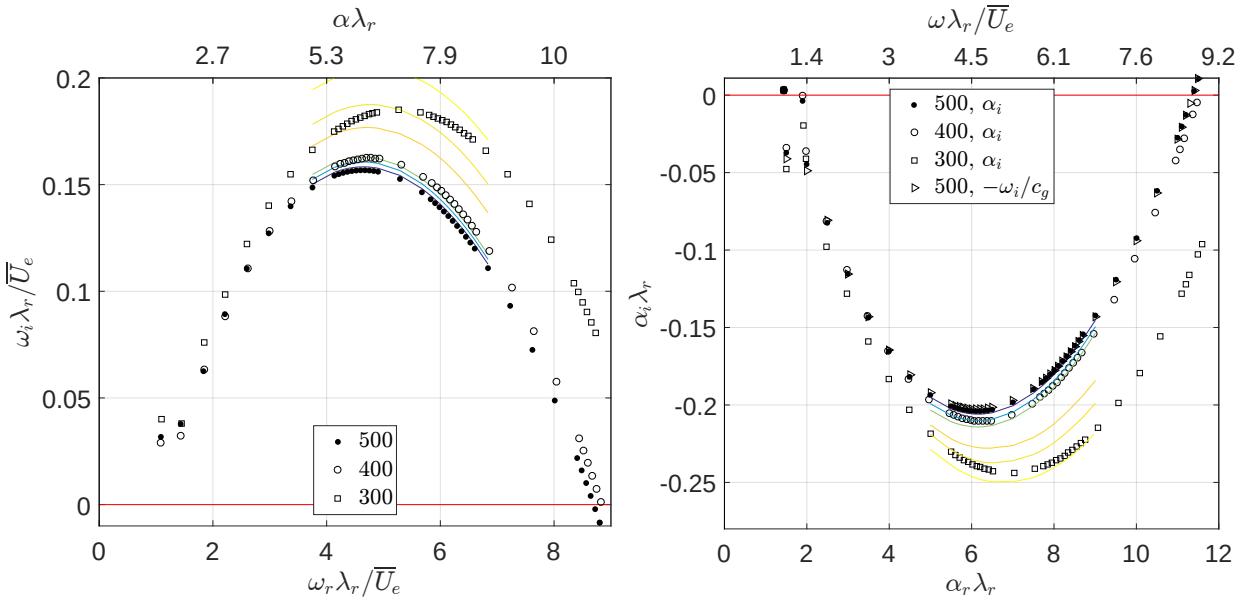

Figure 5. Temporal (left) and spatial (right) eigenvalues associated to the type I secondary instability with varying real α and ω, respectively. The spacing of the latter is chosen so to densely resolve the most unstable and most amplified modes at the $x/c = 45\%$ location. The Gaster-transformed 500 frame temporal spectrum is shown amongst the spatial spectra. Note that the top axes, indicating the input for the 500 frame base flow case, are non-linear. Pseudospectrum levels corresponding to the 500 frame case are superposed, for the temporal spectrum: $10\hat{}(-6, -5, -4, -3.1, -3, -2.9)$ and the spatial spectrum: $10\hat{}(-7, -6, -5, -4.1, -4, -3.9)$.

associated to the PIV base flow datasets lie very far. This is in agreement with the common knowledge that stability results depend very sensitively on the base flow parameters. But this is a pessimistic indication. The disturbance operators yielding the precise movement of an eigenvalue onto the pseudospectrum are very special. It is in no sense clear that the PIV base flow errors are as special. Investigating the actual movement due to the convergence of the mean PIV flow with respect to the pseudo levels helps understanding the impact of using experimentally measured base flows on the stability results for this case specifically. To this end, the pseudospectrum levels are calculated about the type I mode obtained with the 500 frame PIV dataset, so to compare the locations obtained corresponding to the other datasets. Note the use of the 500 frame dataset implies the assumption that that is the "correct" base flow solution. This is *a posteriori* justified regarding the resulting convergence characteristics with respect to the ensemble size. The pseudo levels are computed in the imaginary direction with respect to the eigenvalue as the imaginary part is found to be most sensitive to perturbations. A standard sweep over these pseudospectrum levels is indicated in a single BiGlobal spectrum in Fig. 4(right), indicating the location at which the levels are computed. The pseudo levels themselves in this figure are presented in Fig. 5(left).

IV. Results

The temporal and spatial branches corresponding to the type I mode obtained for a range of α and ω, respectively, are displayed in Figure 5(left) and -(right). The temporal problem is solved for the α-range $[1.5, 11.5]/\lambda_r$ with a spacing of half a unit of $1/\lambda_r$. The most unstable, forced and high frequency neutral modes (respectively having $(\alpha\lambda_r, \omega\lambda_r/\overline{U}_e) = (6.1; 4.6)$, $(8.2; 6.2)$ and $(11.4; 8.7)$) are resolved with a spacing of a tenth unit of $1/\lambda_r$. These α-values are based on the 500 frame base flow case specifically and fixed for the other cases. The obtained real parts of the temporal frequencies are used as the input for the spatial problem. The obtained branches display the characteristic shape associated to the Kelvin-Helmholtz mechanism[35] associated to the type I mode and are qualitatively comparable with computational literature.[1] The closest extracted wavenumbers and frequencies for the comparison to the experimental data are: $(\alpha_r\lambda_r, \omega_r\lambda_r/\overline{U}_e) = (9.5; 7.2)$ for the tomo-PIV and $(8.2; 6.2)$ for the hot-wire experiment. Both frequencies are higher than the most unstable frequencies at this location. This is a qualitative indicator for the spatially most amplified mode, as a frequency attaining the maximal N-factor usually is itself not the most unstable wave at that streamwise location.[36]

Although the statistical uncertainties of the mean flows are large, of $\mathcal{O}(10^{-2.3})$, Fig. 5 shows the resulting

branches are similar over the covered frequency range. The main change is a vertical shift, that increases for higher frequencies and wavenumbers. The real dispersion parameters pertaining to the phase and group speed differ very slightly, the average group speed found for the spatial 500, 400, 300 and temporal 500 frame cases are 0.7725, 0.7760, 0.7648 and 0.7736 units of $\overline{U}_e$, respectively, indicating $\mathcal{O}(10^{-3})$ errors in the real parameters for the 400 and 500 frame cases. These values agree with the values reported by Bonfigli & Kloker,[1] Malik *et al.*[7] and Koch *et al.*[19] The average group speed $c_g = 0.7736\overline{U}_e$ is used for the Gaster-transformation[37] of the 500 frame temporal spectrum shown in Fig. 5(right); which agrees remarkably with the spatial branch. As the number of frames increases, the growth rates ω_i and $-\alpha_i$ decrease and saturate. The same applies to the most unstable real frequency and wavenumber. To quantify the proximity of the branches more closely, specific pseudospectrum contours corresponding to the 500 frame case are shown, combining the levels obtained per mode as described before. The levels are chosen to indicate the contour distributions close to the 300 and 400 frame cases. Most striking is that the 400 frame branch covers the 10^{-4} and 10^{-5} contours in the temporal and spatial spectra, respectively. It lies in the steep valley close to the 500 frame case. This means that the branches are insensitive to the residuals in the mean flows associated to the finite ensemble size. In that sense, these residuals are suboptimal. It is concluded that the effective differences in the 400 and 500 frame cases are of $\mathcal{O}(10^{-4})$ and $\mathcal{O}(10^{-5})$ for the temporal and spatial spectra, respectively. Note that these results cannot be used to quantify the convergence with respect to the ensemble size for the mean; it only indicates that error estimates based on the pseudospectrum are very pessimistic. It is unclear why the pseudo levels for the temporal and spatial problems differ by an order of magnitude. It cannot be the result of using the weighted pseudo-spectrum definition, see Riedel,[34] as the right hand side matrix norm sizes are the same.

Absolute eigenfunction profiles corresponding to the frequency considered in the tomo-PIV experiment are shown in Fig. 6(left). This is the frequency corresponding to the largest differences in the branches. The profiles are shown at the z_w-coordinate where the $|\tilde{u}_w|$-amplitude attains its maximum in the 500 frame case. A first observation is that these profiles have very small magnitudes in the near-wall region and in the freestream. Second, the temporal and spatial eigenfunctions corresponding to the 500 frame case are found to be virtually identical. The same conclusion is drawn when considering the full two-dimensional absolute amplitude contours for all variables. The combination of the match of the temporal and spatial eigenvalues and -functions demonstrates the Gaster-transformation can be applied with confidence. Third, it is found that the profiles corresponding to the 400 and 500 frame cases closely overlap as well. The only noticeable differences are small depressions in the $\tilde{v}$- and $\tilde{w}$-amplitudes of the 400 frame case. This indicates that the 400 and 500 frame base flows yield nearly identical mode structures, although the eigenvalues have slightly different imaginary parts. With these observations it is concluded that the 400 and 500 frame cases yield a converged stability result. The latter will therefore be used to compare to the experimental data in the remainder of the paper. A significant difference is expected when regarding the 300 frame case. This manifests itself primarily in the eigenfunction's maximum moving towards the wall. It is unclear why this happens, as the shear profiles in Fig. 3(right) for the 300 frame case indicates a local increment in the opposite direction.

It is important to quantify the effect of the parameters of the Blasius extrapolation to approach the limited field of view in the experiment. Significant variations in the position (δ_{PIV}) and size (Δy) of the overlap region causes negligible differences. This is displayed in Fig. 6(right). Increasing both δ_{PIV} and Δy reduces the "intrusiveness" with the PIV data, in terms of changing the data inside the field of view and the introduced shear magnitude, respectively. The type I eigenvalue behaves as expected, as the parameters are maximized, the eigenvalue converges and attains $\mathcal{O}(10^{-5})$ absolute convergence levels. The physical reason for this is that the eigenfunctions are small in the near-wall and freestream regions and are hence affected to an insignificant extent. The used overlap region for the results presented in this paper was set to have zero overlap with the PIV domain ($\delta_{PIV} = 0.433\lambda_r$) and the same wall-normal extent as the PIV domain ($\Delta y = 0.433\lambda_r$). This wall-normal extent ensures the shear magnitude introduced in the extrapolated region is small with respect to that inside the PIV domain for this specific case.

The two-dimensional amplitude distributions of the BiGlobal mode are compared to the (total) r.m.s. of the tomo-PIV experiment in Fig. 7. The near-wall region is cut from the experimental data as this is deemed affected too much by measurement noise. The BiGlobal mode is evaluated at $x_w = 0$, while the experimental contours are extracted at $x_w = 17.55\,[mm] = 2.5\lambda_r$. This is done because the measured structures at $x_w = 0$ are deemed to be too small to have been properly captured. Regarding the assumption of x_w-inhomogeneity, it is deemed to have negligible impact on the current comparison. First of all, the relative magnitudes of

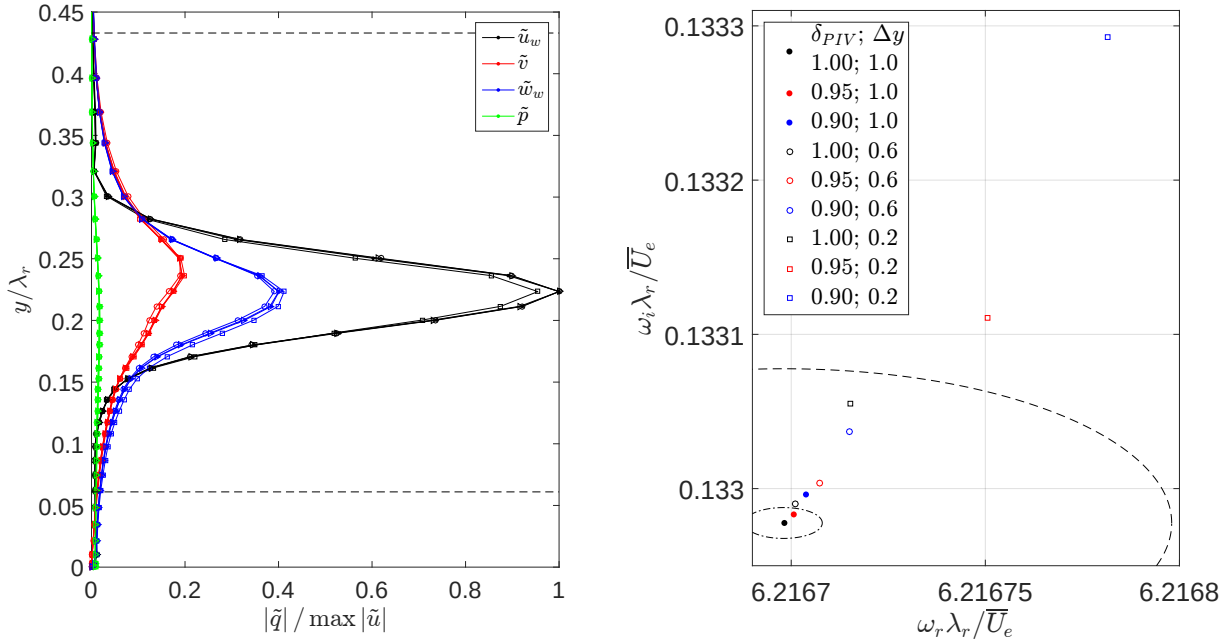

Figure 6. (left) Absolute eigenmode y-profiles at $z_w = 0.378\lambda_r$, where the type I $|\tilde{u}_w|$eigenfunction corresponding to the 500 frame base flow is maximal. The solid dots, circles and squares correspond to the 500, 400 and 300 frame spatial BiGlobal modes (at $(\alpha\lambda_r; \omega\lambda_r/\overline{U}_e) = (9.506 - 0.1191i; 7.228)$, $(9.465 - 0.1319i; 7.228)$ and $(9.572 - 0.1988i; 7.228)$, respectively) and the triangles to the temporal BiGlobal mode for the 500 frame base flow (for $(\alpha\lambda_r; \omega\lambda_r/\overline{U}_e) = (9.500; 7.228 + 0.09318i)$). Black dashed lines indicate the near-wall region and the upper limit of the field of view. (right) Temporal eigenvalue for different domain extrapolation parameters (in units of $0.433\lambda_r$). Dashed and dash-dotted lines indicate 10^{-4} and 10^{-5} absolute error limits with respect to the $\delta_{PIV} = \Delta y = 0.433\lambda_r$ case.

the different velocity components are very close. This is unexpected regarding the apparent sensitivity of the relative magnitudes of the local $\tilde{v}$- and $\tilde{w}_w$-profiles as opposed to $\tilde{u}_w$ displayed in Fig. 6. Second, the structure of the streamwise and wall-normal components agree well, the main difference being the extent. This is remarkable when comparing the uncertainty of the mean $0.1/\sqrt{500} \approx 0.0045$, represented by the non-zero r.m.s. levels in the background, to the size of the $\tilde{v}$ component. It is more difficult to find similarities for the spanwise component. An explanation for these differences could lie in the structure of the most energetic POD mode corresponding to this experimental measurement, reported by Serpieri & Kotsonis.[24] This mode shakes the whole primary vortex in the spanwise direction. Lastly, next to the type I structure, a hint can be detected of another in the x_w-component. Just above the near-wall region, one can see an elevation in the r.m.s. level. If not related to measurement noise, it is most probably related to the top of the type III mode. Similarly, the ring shape about the outer mean flow contour could be associated to the type II mode.

The three-dimensional instantaneous x_w-velocity isosurfaces of the BiGlobal mode are compared to those of the POD mode that is representative of the type I mode from the tomo-PIV experiment in Fig. 8. Using the x_w-inhomogeneity argument, the spatial BiGlobal mode is extrapolated in space, incorporating the spatial growth. A difference is the absence of surfaces upstream of the $x_w = 0$ station in the POD mode. This is associated to the limited dynamic range of this particular tomo-PIV experiment. Overall, accounting for the logical and explainable differences in the structure in the different representations, the structures match. Based on this comparison, it is difficult to conclude whether the linear spatial growth matches with the experiment; further investigations have to be undertaken to pinpoint this.

A similar representation of the type I mode's structure is shown in Fig. 9, where it is compared against the phase-locked hot-wire measurements. Recall that the BiGlobal analysis is applied to the base flow conceived from the tomo-PIV experiment, so this implies an extrapolation from one to another experiment. A 4 $[kHz]$ forcing was applied in the hot-wire experiments, different with respect to the 5 $[kHz]$ center of the bandpass range for the POD mode. The irregularity in the measurement isocontours is due to the small number of measured phases, 10, in the phase-locking procedure. Here, the spatial BiGlobal mode is extrapolated in time, at a fixed position, so no growth is involved. Note, that the figure is represented in the leading edge parallel z-coordinate, while the x_w-velocity isosurface is depicted. The isocontour levels are equated to the

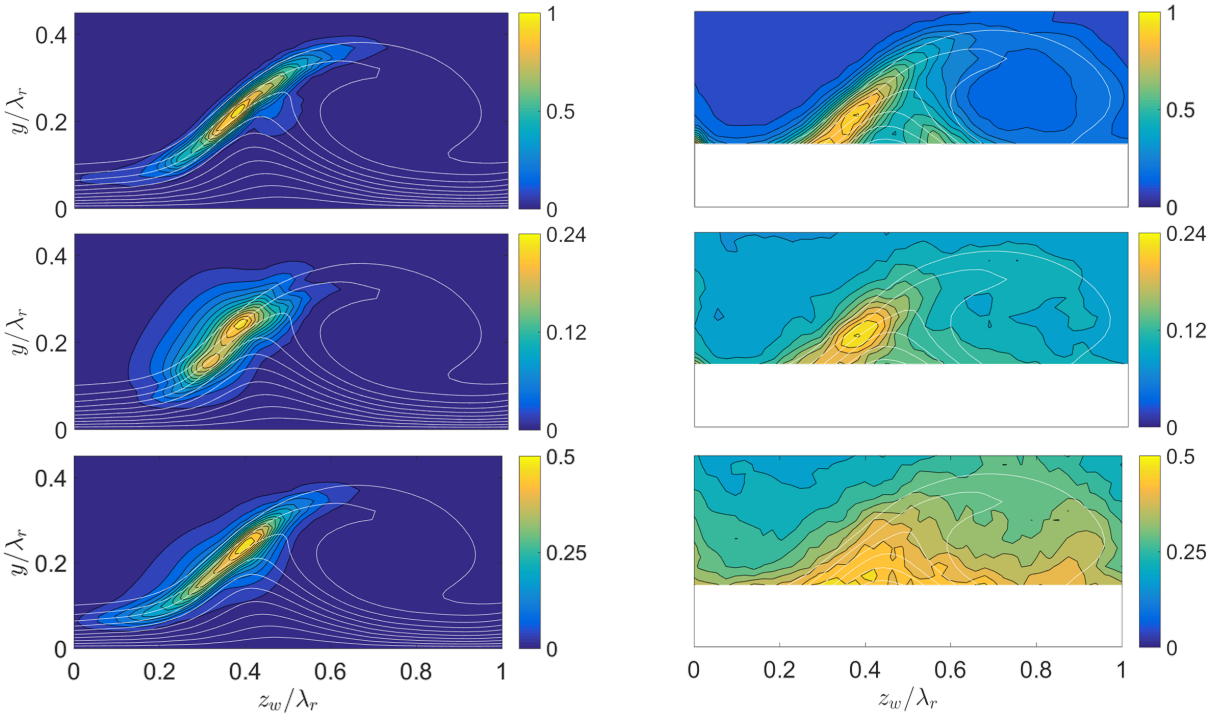

Figure 7. Relative magnitudes of the (top) x_w-, (middle) y- and (bottom) z_w-velocities of (left) the type I spatial BiGlobal mode with $(\alpha\lambda_r; \omega\lambda_r/\overline{U}_e) = (9.506 - 0.1191i; 7.228)$ at $x_w = 0$ and (right) the r.m.s. of the tomo-PIV measurement at $x_w = 17.55\,[mm]$, the region affected by the wall proximity is cut. 15 base flow contours are superposed ranging from 0 to $\overline{U}_e$.

measured relative magnitude with respect to the maximum perturbation level. Again, the structures are found to be very similar. In this case, variations in the size of the structure can be directly compared and agree qualitatively.

V. Discussion

Stability equations are differential equations having the base flow velocity fields and their derivatives as their coefficients. The velocity derivatives strongly influence the results and therefore must be determined up to high accuracy.[2] The only consistent, though practically vague, argument in this regard is that the fields should satisfy the Navier-Stokes equations.[14] In practice, one uses the condition that the stability results have to be converged with the numerical parameters of the laminar base flow solution, at least to the required accuracy. To satisfy this condition, highly refined high-fidelity computational methods are usually deployed, just to make sure base flow errors are absolutely minimal.

Applying stability analysis to experimentally measured base flows is a controversial topic. Letting alone resolution, the closest one can get to the laminar undisturbed flow is to regard the mean of instantaneous fields as a close representation. These resulting flow fields include a residue of the perturbation field and measurement noise, so one violates the requirement of it being a laminar Navier-Stokes solution. The residual perturbation field consists, for example, of Reynolds stress effects and residues related to finite ensembles. The perturbations of interest here are small and mono-chromatic. So, the only, in itself negligibly small, non-linear effect they can exert is self-interaction. Hence, the disturbance dynamics is linear up to good approximation and it can be assumed to have a negligible effect on the laminar flow. In short, Reynolds stresses can be assumed to be negligible. This implies that, as long as measurement noise and the residuals due to the mean's ensemble size are small enough, one can use the measured mean flow field as a base flow. Regarding these premises, this approach is consistent. Examples of applications of stability theory that are strictly inconsistent apply it to turbulent flows where Reynolds stresses cannot be neglected.[38]

Applying stability methods to experimental data also has definite advantages. One can think of problems for which the experimental set-ups are standard and cheap, while the corresponding computational approach requires months of expensive CPU time on clusters. Furthermore, parameter uncertainty and important

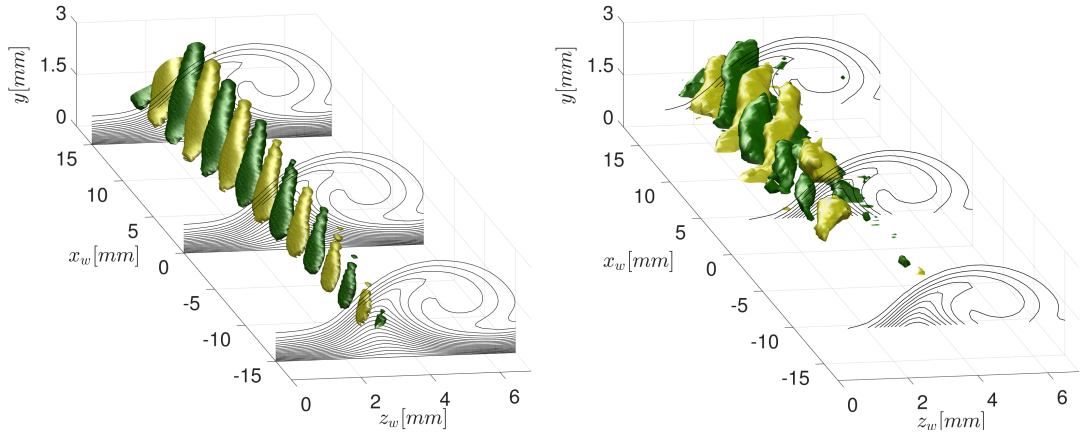

Figure 8. x_w**-velocity isosurfaces of (left) the type I spatial BiGlobal mode at the frequency** $\omega/2\pi = 5\,[kHz]$ **(**$\alpha_r = 9.5/\lambda_r$**), having maximal amplitude 1 at** $x = -17.6\,[mm]$**, plotting the** $\pm 84\%$ **levels, and (right) the tomo-PIV POD mode, plotting the** $\pm 0.086\overline{U}_e$ **levels, the near-wall region is cut.**

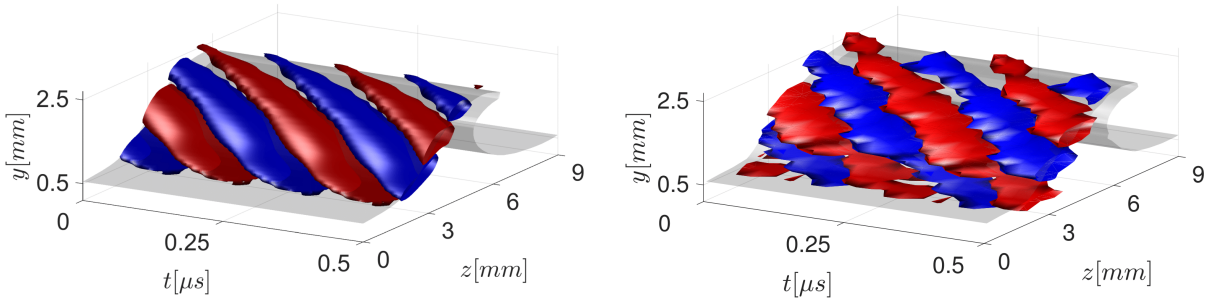

Figure 9. 2 periods of the perturbation (red and blue) and mean (grey) x_w**-velocity isosurfaces of (left) the type I spatial BiGlobal mode (**$\pm 18\%$ **of the maximum amplitude) at the frequency** $\omega/2\pi = 4.0\,[kHz]$ **(**$\alpha_r = 8.2/\lambda_r$**) and 500 frame tomo-PIV mean flow (**$23\,[m/s]$**) and (right) the phase-locked hot-wire fluctuations (**$\pm 0.5\,[m/s]$**) forced with** $f_f = 4.0\,[kHz]$ **and the time-averaged field (**$20\,[m/s]$**).**

details specifically associated to the experimental environment are covered as closely as possible. One could argue that, if the stability results are that sensitive to the base flow, one might have to incorporate (or at least model) all these specific features to match the experimental situation. Take the spanwise periodicity as an example. The strength of the primary vortices varies along the span, according to the specific roughness receptivity and freestream turbulence level. These effects are accounted for as realistically as possible in an experimentally measured base flow. Efficiently replicating this kind of experimental environment is very difficult. Lastly, the practical approach to transition has always combined stability methods with experiments; leading to e^N-correlations. The current approach brings the stability method closer to the experiment, making the potential mismatch smaller.

The current approach is feasible for other fundamental reasons. It is hard to obtain high quality measurement data near the wall; the near-wall region is where experimental noise is non-negligible. The secondary instabilities of main interest here are driven by inviscid mechanisms. Inviscid instabilities are localized about the inflection points in shear layers and, in this case, this point lies far away from the wall, so it can be measured well with Particle Image Velocimetry (PIV). Near-wall details, especially wall-normal shear, are more difficult to acquire for practical reasons like reflections. This means that applying this approach to wall-bounded viscous instabilities like TS waves is more challenging.

Furthermore, the current secondary instabilities appear as discrete modes in the BiGlobal spectra. This means that they are "global modes," in the sense associated to the spanwise BiGlobal domain.[39] A global modes' direct eigenfunction must, at least partially, overlap the associated adjoint eigenfunction. The adjoint eigenfunction indicates the region of influence of the mode.[40] The necessity of the overlap suggests that the adjoint eigenfunction, just like the direction eigenfunction, is small in the near-wall region. Hence, the experimental noise in the near-wall region has negligible influence on the mode. The actual extent of the adjoint eigenfunction has to be determined to investigate this in more detail.

For these two reasons the general methodology of applying stability theory to measured base flows is expected to be feasible at least for these inviscid perturbations that live about inflection points far from the wall.

VI. Conclusion

BiGlobal stability theory is applied to resolve secondary instability of swept-wing three-dimensional boundary layers. The treatment is focussed on the type I mode as this is the most dominant. The stability results are found to be converged with the ensemble size of the mean tomo-PIV flow. Pseudo spectrum levels indicate that, although the statistical uncertainty of the mean is rather high ($\mathcal{O}(10^{-3})$), the residual differences between the 400 and 500 frame datasets effectively correspond to differences of $\mathcal{O}(10^{-4})$ for the temporal and $\mathcal{O}(10^{-5})$ for the spatial approach. It is moreover found that the treatment of the freestream and, hence, the near-wall region has negligible effect on the stability results, which is associated to the negligible amplitude of the eigenfunctions in these regions.

This indicates, at least for this application, that resolving the shear layers associated to the secondary instabilities is sufficient to be able to perform stability analysis. Inherently, this implies that by measuring the primary crossflow vortices to sufficient detail, using tomo-PIV, it is possible to capture the secondary instability via stability analysis and use it for classical secondary e^N transition correlations. Thereby one circumvents having to scrutinize the delicate primary vortices' receptivity in the computational approach.

It is found that the temporal and spatial eigenfunctions display the same absolute profiles. The spatial eigenfunctions corresponding to the 500 and 400 frame datasets are very similar, the main difference being the relative proportion of the $\tilde{v}$ and $\tilde{w}_w$ amplitudes with respect to $\tilde{u}_w$.

Successful validations are performed with respect to the instantaneous tomo-PIV and hot-wire measurement data for the frequencies associated to the measured structures. Comparing the spanwise amplitude distributions, high similarity is observed, despite the apparent sensitivity of the $\tilde{v}$ and $\tilde{w}_w$-profiles. The three-dimensional structures, in turn display a high degree of similarity.

References

[1]Bonfigli, G. and Kloker, M., "Secondary instability of crossflow vortices: validation of the stability theory by direct numerical simulation," *Journal of Fluid Mechanics*, Vol. 583, 2007, pp. 229.

[2]Reed, H. L., Saric, W. S., and Arnal, D., "Linear Stability Theory Applied to Boundary Layers," *Annual Review of Fluid Mechanics*, Vol. 28, No. 1, 1996, pp. 389–428.

[3]Saric, W. S., Reed, H. L., and White, E. B., "Stability and Transition of three-dimensional boundary layers," *Annual Review of Fluid Mechanics*, Vol. 35, No. 1, jan 2003, pp. 413–440.

[4]White, E. B. E. and Saric, W. W. S., "Secondary instability of crossflow vortices," *Journal of Fluid Mechanics*, Vol. 525, 2005, pp. 275–308.

[5]Van Ingen, J. L., "The e^N-method for transition prediction. Historical review of work at TU Delft," *38th Fluid Dynamics Conference & Exhibit*, No. 2008-3830, AIAA, ISBN: 978-1-60086-989-1, Seattle, Washington, June 2008.

[6]Malik, M. R., Li, F., and Chang, C.-L., "Crossflow disturbances in three-dimensional boundary layers: nonlinear development, wave interaction and secondary instability," *Journal of Fluid Mechanics*, Vol. 268, No. -1, 1994, pp. 1.

[7]Malik, M. R. M., Li, F., Choudhari, M. M. M., and Chang, C.-L. L., "Secondary instability of crossflow vortices and swept-wing boundary-layer transition," *Journal of Fluid Mechanics*, Vol. 399, 1999, pp. 85–115.

[8]Kohama, Y., Saric, W., and Hoos, J., "A high frequency, secondary instability of crossflow vortices that leads to transition," *Proc. R. Aeronaut. Soc. Conf. on Boundary-Layer Transition and Control, Cambridge, UK*, 1991.

[9]Kawakami, M., Kohama, Y., and Okutsu, M., "Stability characteristics of stationary crossflow vortices in three-dimensional boundary layer," 1998.

[10]Bippes, H. and Lerche, T., "Transition prediction in three-dimensional boundary-layer flows unstable to crossflow instability," *AIAA paper*, Vol. 1906, 1997, pp. 1997.

[11]Bippes, H., "Basic experiments on transition in three-dimensional boundary layers dominated by crossflow instability," *Progress in aerospace sciences*, Vol. 35, No. 4, 1999, pp. 363–412.

[12]Chernoray, V. G., Dovgal, A., Kozlov, V. V., and Löfdahl, L., "Secondary instability of a swept-wing boundary layer disturbed by controlled roughness elements," *Journal of visualization*, Vol. 13, No. 3, 2010, pp. 251–256.

[13]Glauser, M. N., Saric, W. S., Chapman, K. L., and Reibert, M. S., "Swept-wing boundary-layer transition and turbulent flow physics from multipoint measurements," *AIAA journal*, Vol. 52, No. 2, 2014, pp. 338–347.

[14]Theofilis, V., "Advances in Global Linear Instability Analysis of Nonparallel and Three-Dimensional Flows," *Progress in Aerospace Sciences*, Vol. 39, No. 4, 2003, pp. 249–315.

[15]Högberg, M. and Henningson, D., "Secondary instability of cross-flow vortices in Falkner–Skan–Cooke boundary layers," *Journal of Fluid Mechanics*, Vol. 368, 1998, pp. 339–357.

[16]Wassermann, P. and Kloker, M., "Mechanisms and passive control of crossflow-vortex-induced transition in a three-dimensional boundary layer," *Journal of Fluid Mechanics*, Vol. 456, 2002, pp. 49–84.

[17]Herbert, T., editor, *Finite amplitude stability of plane parallel flows*, Oct. 1977.

[18]Janke, E. and Balakumar, P., "On the secondary instability of three-dimensional boundary layers," *Theoretical and Computational Fluid Dynamics*, Vol. 14, No. 3, 2000, pp. 167–194.

[19]Koch, W., Bertolotti, F. P., Stolte, A., and Hein, S., "Nonlinear equilibrium solutions in a three-dimensional boundary layer and their secondary instability," *Journal of fluid mechanics*, Vol. 406, 2000, pp. 131–174.

[20]Malik, M. R., Li, F., and Chang, C.-L., *Nonlinear Crossflow Disturbances and Secondary Instabilities in Swept-Wing Boundary Layers*, Springer Netherlands, Dordrecht, 1996, pp. 257–266.

[21]Fischer, T. and Dallmann, U., "Primary and secondary stability analysis of a three-dimensional boundary-layer flow," *Physics of Fluids A: Fluid Dynamics (1989-1993)*, Vol. 3, No. 10, 1991, pp. 2378–2391.

[22]Groot, K. J., Ye, Q., van Oudheusden, B., Zhang, Y., and Pinna, F., "BiGlobal Stability Analysis of a Micro-Ramp Wake using PIV Base Flows," *AIAA* Paper 2016, June 2016.

[23]Scarano, F., "Iterative image deformation methods in PIV," *Measurement science and technology*, Vol. 13, No. 1, 2001, pp. R1.

[24]Serpieri, J. and Kotsonis, M., "Three-dimensional organisation of primary and secondary crossflow instability," *J. Fluid Mech.*, Under revision.

[25]Serpieri, J. and Kotsonis, M., "Spatio-temporal characteristics of secondary instabilities in swept wing boundary layers," *AIAA Paper*, 2016.

[26]Sirovich, L., "Turbulence and the dynamics of coherent structures part I: coherent structures," *Quarterly of applied mathematics*, Vol. 45, No. 3, 1987, pp. 561–571.

[27]Cossu, C. and Brandt, L., "On TollmienSchlichting-like waves in streaky boundary layers," *European Journal of Mechanics-B/Fluids*, 2004.

[28]Groot, K. J., Pinna, F., and Van Oudheusden, B. W., "On closing the streamwise BiGlobal stability problem: the effect of boundary conditions," *8th IUTAM-ABCM Symposium on Laminar-Turbulent Transition*, Elsevier, Rio de Janeiro, 2014.

[29]Pinna, F., *Numerical study of stability of flows from low to high Mach number*, Ph.D. thesis, Università di Roma- "La Sapienza", Von Kármán Institute, Rhode-Saint-Genèse, 2012.

[30]Malik, M. R., "Numerical methods for hypersonic boundary layer stability," *Journal of Computational Physics*, Vol. 86, No. 2, 1990, pp. 376–413.

[31]Wheeler, P. and Barkley, D., "Computation of spiral spectra," *SIAM Journal on Applied Dynamical Systems*, Vol. 5, No. 1, 2006, pp. 157–177.

[32]Reddy, S. C., Schmid, P. J., and Henningson, D. S., "Pseudospectra of the Orr-Sommerfeld operator," *SIAM Journal on Applied Mathematics*, Vol. 53, No. 1, 1993, pp. 15–47.

[33]Trefethen, L. N. and Embree, M., *Spectra and pseudospectra: the behavior of nonnormal matrices and operators*, Princeton University Press, 2005.

[34]Riedel, K. S., "Generalized epsilon-pseudospectra," *SIAM journal on numerical analysis*, Vol. 31, No. 4, 1994, pp. 1219–1225.

[35]Drazin, P. G. and Reid, W. H., *Hydrodynamic Stability*, Cambridge University Press, ISBN: 978-0521525411, 2004.

[36]Arnal, D., "Boundary Layer Transition: Predictions Based on Linear Theory," *Special course on Progress in Transition Modelling*, No. R-793, AGARD, ISBN: 92-835-0742-8, 1994.

[37]Gaster, M., "A note on the relation between temporally-increasing and spatially-increasing disturbances in hydrodynamic stability," *Journal of Fluid Mechanics*, Vol. 14, 1962, pp. 222–224.

[38]Jordan, P. and Colonius, T., "Wave packets and turbulent jet noise," *Annual review of fluid mechanics*, Vol. 45, 2013, pp. 173–195.

[39]Huerre, P. and Monkewitz, P., "Local and Global Instabilities in Spatially Developing Flows," *Annual Review of Fluid Mechanics*, Vol. 22, No. 1, 1990, pp. 473–537.

[40]Luchini, P. and Bottaro, A., "Adjoint equations in stability analysis," *Annual Review of fluid mechanics*, Vol. 46, No. 1, 2014, pp. 493.